Projectilelike fragment emission angles in fragmentation reactions of light heavy ions in the energy region <200 MeV/nucleon: Modeling and simulations

M. Giacomelli,[1,2,*] L. Sihver,[2,3] J. Skvarč,[4] N. Yasuda,[5] and R. Ilić[1,6]

[1]*Department of Reactor Physics, Jožef Stefan Institute, Jamova 39, 1000 Ljubljana, Slovenia*
[2]*Department of Materials and Surface Chemistry, Nuclear Science and Technology, Chalmers University of Technology, SE-412 96, Göteborg, Sweden*
[3]*Roanoke College, Department of Physics, 221 College Lane, Salem, Virginia 24153, USA*
[4]*Jožef Stefan Institute, Department of Reactor Physics, Jamova 39, 1000 Ljubljana, Slovenia*
[5]*International Space Radiation Laboratory, National Institute of Radiological Sciences, 4-9-1 Anagawa, Inage-ku, Chiba 263-8555, Japan*
[6]*Faculty of Civil Engineering, University of Maribor, Smetanova 17, 2000 Maribor, Slovenia*

A new semiempirical model called FRANG for calculation of fragment emission angles in light and heavy ion fragmentation reactions was developed. Contributions from both central and peripheral collisions were investigated, where fragmentation occurs due to nuclear and Coulomb interaction, respectively. For central collisions the reaction was described by a two step abrasion-ablation model, where collision parameters were determined from a simple geometrical model. The fragment emission angles were calculated using a parametrization of longitudinal momentum loss and transverse momentum uptake in the collision of projectile and target atom. For peripheral collisions the Coulomb excitation of nucleon vibration resonances and subsequent decay into fragments was taken into account. Fragment emission angles were calculated from deflection in the electric field and from the amplitude of vibrations in excited nuclear states. The modeled emission angles were in accordance with the experimental values for most projectile-target systems examined and compared. It was established that the model very well reproduces the experimental results in the energy region <200 MeV/nucleon, despite its simplicity, and can be successfully employed in several applications. The model is estimated to be valid in the energy range from a few 10 MeV/nucleon up to few 100 MeV/nucleon.

I. INTRODUCTION

Concern about the biological effects of space radiation is increasing rapidly in view of the perspectives of long-term space missions, both in relation to the International Space Station and to manned interplanetary missions in future years. Galactic cosmic rays (GCR's) and Solar particle events (SPE's), e.g., showers of energetic charged particles from the surface of the Sun will be the dominant sources of the radiation dose on long-term missions outside the Earth's magnetic field and this presents a major risk to human crews. Radiation protection studies of airplane crews on high-altitude long-distance flights have also received considerable attention in recent years.

High-energy heavy-charged (HZE) particles are used in various fields of nuclear physics, medical physics, space science, and materials science. Several ion accelerator facilities are operating or planned for construction.

A major advantage when using hadrons (light and heavy ions) over conventional radiation (photons, electrons) for radiotherapy is the inverse dose profile, i.e., the energy deposition and dose distribution increases along the penetration depth of the beam ending with a sharp maximum—the Bragg peak—at the end of the particle range. HZE particles also produce a very narrow penumbra in the beam due to their reduced scattering angles.

There is an intense ionization pattern along the path of the hadrons, most notably at the end of the range, which results in localized bursts of energy deposition at the microscopic level. This results in increasing cell mortality and thus the radiobiological effect of hadrons is superior to that of conventional radiotherapy, even in conditions of hypoxia. Radioresistant tumors which have a high repair capacity with respect to photon irradiation are susceptible to hadron treatment. In addition to that, light ions exhibit more precise physical dose distributions than protons because lateral and range scattering decreases quadratically with atomic number.

The understanding of the radiobiology of heavy-charged particles is still a subject of great interest due to the complicated dependence of their relative biological effectiveness (RBE) on the type of ion and its energy, and its interaction with various targets. Reviews on radiological effects of HZE particles can be found in Refs. [1,2], and references therein. Calculations of the ion track structure and its localized energy deposition at microscopic level are required in order to establish a correlation between the imparted energy in small sites with single and double strand breaks, base damage, etc., following the very rapid energy-deposition processes and the ensuing chemistry in the cellular environment. At high energies a large number of nuclear interactions occurs producing a cascade of other ions and particles, building complicated spectra of particles which are transported along the path of the initial projectiles. It has become clear that heavy ions such as neon, used during the pioneer application of heavy

*Electronic address: marko.giacomelli@ijs.si

ions for radiotherapy (LBNL, Berkeley, USA) in the early 1970's, have the largest radiobiological effects. These effects also appear in regions close to the beam entrance, i.e., in the depth-dose plateau region, where normal tissue is usually situated. In addition, due to the longer range of the fragmentation products released by the incident ions, the tail of the dose distribution beyond the Bragg peak may be too high for minimizing doses to normal tissue beyond the primary ion range. These two aspects suggest that the ideal ions for radiotherapy are light ions, and for this reason carbon has dominated clinical applications at the HIMAC (NIRS) clinical facility (Chiba, Japan) [3,4], as well as HIBMC (Harima Science Garden City, Hyogo, Japan), and at GSI (Darmstadt, Germany) [5]. Plans for building additional radiotherapy light ion facilities have followed in Europe and China, and new feasibility studies have been conducted for such facilities in Germany, Austria, Italy, France, and Sweden.

In order to estimate the biological effects of HZE particles, accurate knowledge of the physics of interaction of these particles with target atoms is needed. To estimate the exposure of personnel on space missions, the dose absorbed by patients during cancer treatment, and to design the shielding of accelerator and reactor facilities, the interaction and transport of these particles in a medium, including human tissue, should therefore be well understood. For therapeutic and diagnostic medicine, the ability to perform precise three-dimensional calculations of the transport of both primary and secondary particles in biological materials is needed. In the field of Monte Carlo transport of heavy ions several codes (e.g., FLUKA, GEANT, SHIELD, and PHITS) exist and/or are in the stage of development. A major drawback is that often their lowest possible energy, where simulations are still accurate, almost coincides with the initial energies used in radiotherapy ($\sim$500 MeV/nucleon). Additionally, these codes are based on approximations which are unjustified at lower energies. For a long time the only verified numerical HZE transport code has been HZETRN, developed at NASA Langley Research Center [6]. This code is based on semiempirical models, and is only a one-dimensional discrete steps calculation code. Another numerical one-dimensional semi-empirical computer code is HIBRAC [7], developed to support the heavy-ion therapy programs at HIMAC and GSI. This code enables calculation of the fluence, energy, LET, dose, and dose average LET distributions for protons and light ions in any solid and liquid medium. HIBRAC was carefully benchmarked with measurements performed at different accelerators around the world, including GSI and RIKEN (Japan), and then incorporated in the treatment planning systems at HIMAC and GSI.

Our recent measurements [8] have revealed that fragments are emitted at larger angles (several degrees) than previously expected, and therefore the straight-ahead approximation used in HZETRN and HIBRAC seems to be oversimplified, especially in the energy region below 100 MeV/nucleon. Exact information about the fragment emission angular distributions will be especially important in the near future, when so-called pencil beams for precise local irradiation will be brought in operation [9,10]. So far only a few measurements have been performed to analyze fragment emission angles from HZE reactions below 500 MeV/

nucleon [8,11–13]. Analysis was performed mostly for energies above a few GeV/nucleon [14–17]. For this reason we started a series of experiments to determine the angular distributions of various projectiles colliding with targets made of materials important in radiotherapy and space radioprotection. Since no semiempirical model for calculation of fragment emission angular distributions has proved able to reproduce accurately several measured fragment angular distributions, we developed a new semi-empirical model called FRANG to describe the angular emission of fragments when colliding with target atoms. The main goal was to incorporate this model into HIBRAC, together with improved models for calculation of stopping power and cross sections, in order to develop a fast modified three-dimensional version of HIBRAC. However, the FRANG model can also be incorporated in the Monte Carlo codes. Since it is not possible to measure the composition of these transported radiation fields inside internal organs of biological test specimens, or humans, computational methods rather than direct measurements are required.

The scenario of a collision between two heavy nuclei in the energy range from a few 10 MeV/nucleon up to a few GeV/nucleon is very complex. The main nuclear collision processes involved are (i) nuclear elastic and inelastic collisions, (ii) nuclear fragmentation (spallation), and (iii) electromagnetic dissociation (EMD). Only the latter two, (ii) and (iii), change the composition of the treatment beam. Sections II and III are thus dedicated to direct and peripheral collisions, in which fragments are produced through nuclear and Coulomb interactions, respectively. However, we introduce our model for application to space and radiotherapy research, where mainly light ion systems can be found. Within this scope it was established that the main contributor to fragment production is nuclear interaction (by several orders of magnitude). The Coulomb dissociation probability is increased only for highly charged systems (e.g., Pb+Pb) or at relativistic energies (above a few 10 GeV/nucleon).

II. DIRECT COLLISIONS

When two colliding nuclei first touch each other they are cold. In the well-known geometric abrasion-ablation fragmentation model of Bowman *et al.* [18], when the fragmenting projectile nucleus collides with a stationary target nucleus, the overlapping portions of their nuclear volumes are sheared off by the collision. The remaining piece of projectile or target matter, called a prefragment, continues on its initial trajectory with its precollision velocity. In the early stage of the collision the nuclear matter will be a compressed. Because of collisions between the constituent nucleons of the colliding nuclei both the temperature and the entropy will rise. At an intermediate stage a compressed and hot zone of nuclear matter exists, and it is believed [19] that in this system densities of 2–3 times normal nuclear density can be reached. After the initial compression the system expands and the final state of both projectile and target nucleus is reached in one of the following ways: either the excited prefragments are thermalized or they disintegrate into fragments and nucleons.
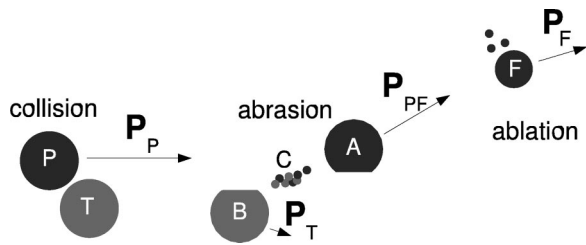
FIG. 1. Abrasion-ablation reaction scheme and corresponding momenta at different steps. The two-nucleon collision system ($P+T$) is partitioned into three parts: projectile spectators (A), target spectators (B), and participant system (C) according to the fireball model [20].
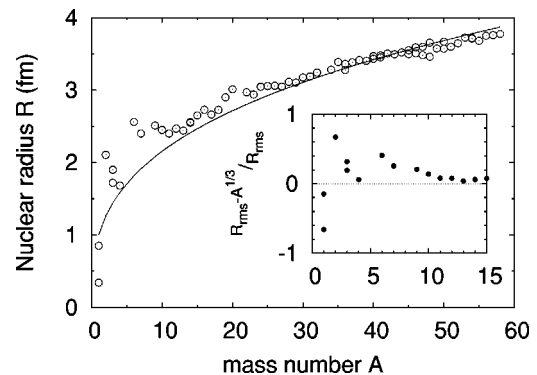

FIG. 2. Accuracy of the nuclear radii parametrization. The full line depicts the approximation of $R = r_0 A^{1/3}$ type, while the symbols depict measured values [26,27]. The inset represents the relative accuracy of the radii parametrization. Large discrepancies can be observed especially for light nuclei.

Because of the dynamics of abrasion, the prefragments are highly excited and decay by emitting nuclear particles and/or γ rays (ablation process). The entire abrasion-ablation process takes less than 10^{-14} s [21]. The resulting isotopes are the nuclear fragments whose production cross sections are used as inputs into the transport code.

In the present model the emission angles are calculated by determining the range of impact parameters that result in the formation of a fragment with specific mass. In the current model we describe only the behavior of projectilelike fragments. This new semiempirical model is based on the models of Fai and Randrup [22,23] and Tsao et al. [24]. The collision is described by a two step abrasion-ablation model, where first an excited prefragment is formed and later a stable reaction product is formed through nucleon or photon emission. In the collision a momentum transfer occurs in both longitudinal and transverse directions. The momentum transfer is taken to be dependent on the projectile energy, impact parameter, and projectile-target combination.

Basic models of the propagation of light ions through matter make a simplifying assumption that fragmentation products retain the same velocity as their progenitors. The straight-ahead approximation would correspond to a δ-function distribution centered at the origin in the projectile's energy in the laboratory reference frame. In the present model the approximation is relaxed by a simple microscopic prescription [22–24]. We estimate that the model is applicable down to lower energies of a few 10 MeV/nucleon. The high-energy end of the model is above few GeV/nucleon. However, at these energies the momentum change of fragments becomes very small compared to the total momentum of the projectile (by a few orders of magnitude). Hence, the modelled values of fragment emission angles resemble the straight-ahead approximation.

Because we use geometrical approximations, the model is more accurate for heavier systems, for which the approximation is more adequate. Similarly, better agrrement with experimental values is expected for heavier fragments (with mass and charge close to the projectile nucleus) and the model cannot be used for description of very light ejectiles, i.e., neutrons and protons.

A. Abrasion partitioning

Let us consider a colliding system consisting of projectile ion and target atom (Fig. 1). In the abrasion step the nuclei

overlap and nucleons are knocked out of their bound orbits. Thus, the system is partitioned into three parts: projectile spectators, target spectators, and participant nucleons. We get

$$A = A_P \mathcal{P}\left(\frac{R_P}{R_T}, b, E\right),$$

$$B = A_T \mathcal{P}\left(\frac{R_T}{R_P}, b, E\right),$$

$$C = A_P + A_T - (A + B), \tag{1}$$

where A_P, A_T, A, B, and C are the projectile, the target, the projectile spectators, the target spectators, and the participant mass numbers, respectively. For A, B, and C integer values are taken. E is the kinetic energy of the projectile. $\mathcal{P}$ represents a set of geometric approximation functions for the overlap volume of the projectile-target system. Functions $\mathcal{P}$ are listed in Ref. [25]. Values of the radii of the colliding nuclei, R_P and R_T for projectile and target, respectively, are taken as the root-mean-square values measured by de Vries et al. [26] and Wesołowski [27]. In the literature, approximations of $R = r_0 A^{1/3}$ type are commonly used (e.g., $r_0 = 1.2$ fm). However, these approximations are only good for heavier nuclei. Discrepancies of up to 50% for light nuclei are clearly demonstrated in Fig. 2. Thus measured radii values are used throughout this paper. The number of participants and spectators at a given impact parameter b, calculated according to the functions $\mathcal{P}$, is corrected and taken to be energy (E) dependent as proposed by Wilson et al. [28]. In Fig. 3 these corrections are shown at different energies. The charge of the three parts is distributed under the assumption that the ratio of the number of protons and neutrons is maintained
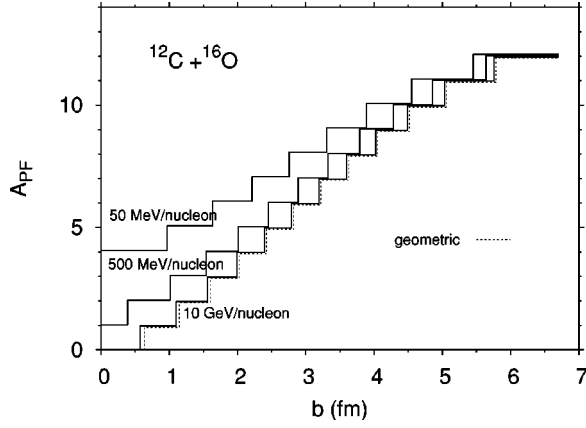
FIG. 3. Calculation of the number of projectile spectator nucleons at different energies. The dotted line represents simple geometric approximation.

$$Z_A \approx A \frac{Z_P}{A_P},$$

$$Z_B \approx B \frac{Z_T}{A_T},$$

$$Z_C = Z_P + Z_T - (Z_A + Z_B). \tag{2}$$

Next we partition the total momentum before the collision among the sources in the center-of-mass frame (in which $\mathbf{P}_P + \mathbf{P}_T = 0$). After the abrasion the parallel components are written as

$$P_{\parallel A} = (1 - y) \frac{A}{A_P} P_P,$$

$$P_{\parallel B} = (1 - y) \frac{B}{A_T} P_T,$$

$$P_{\parallel C} = -(P_{\parallel A} + P_{\parallel B}). \tag{3}$$

The parameter $y \in [0, 1]$ is a measure of the reduction of motion of spectators. When $y = 0$ spectators continue with their initial momentum per nucleon (reducing the model to the straight-ahead approximation), while when $y = 1$, all three sources move with the same velocity (in the laboratory system). The parameter y is somewhat analogous to the inelasticity parameter used to characterize two-body collisions. Transverse components of the three sources also satisfy the criterion

$$P_{\perp A} + P_{\perp B} + P_{\perp C} = 0. \tag{4}$$

Finally, the generated heat Q, equal to the loss of translational energy implied by Eq. (3), should be partitioned. In the standard fireball model [20] all the heat Q goes into the participant source while the spectators remain cold. Here, a parameter $x \in [0, 1]$ is employed to govern the leakage of heat into the spectators. Thus, the assumption is made that the invariant source mass energies are given by
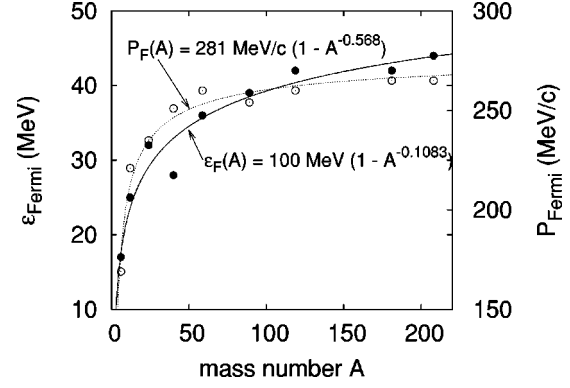

FIG. 4. Measured Fermi momentum (open symbols) and energy (full symbols) [32]. The full and dashed lines represent the best fitted function for energy and momentum, respectively.

$$M_A = m_A c_o^2 + Axq,$$

$$M_B = m_B c_o^2 + Bxq,$$

$$M_C = m_C c_o^2 + C \left(1 + \frac{A + B}{C} (1 - x) \right) q, \tag{5}$$

where m_i are the relative atomic masses of the isotopes $i = (A, B, C)$ [29]. For the spectator part C, m_C is taken either as the mass of an existing nucleon or as the mass sum of a cluster of separate neutrons and/or protons. q is the excitation energy per nucleon

$$q = \frac{Q}{A_P + A_T}. \tag{6}$$

When $x = 0$ there is no leakage of heat into spectators, and the participant source takes all the generated excitation energy. On the other hand, when $x = 1$, excitation per baryon, and hence the temperature, is the same in all three sources, corresponding to perfect heat sharing.

In this model Eqs. (1)–(3) are set to conserve baryon number, charge, and momentum. Energy conservation is ensured by

$$E_P + E_T = E_A + E_B + E_C, \tag{7}$$

where the source energies are $E_i^2 = P_i^2 c_o^2 + M_i^2 c_o^4$ and $i = (P, T, A, B, C)$.

The generated heat in Eq. (5) is obtained by iterating Eq. (7) starting with $Q^{(k)} = 0$. An improved approximation is given by

$$Q^{(k+1)} = Q^{(k)} + E_P + E_T - (E_A^{(k)} + E_B^{(k)} + E_C^{(k)}). \tag{8}$$

It was assumed that the two spectators are excited in proportion to their mass ratio, i.e., $Q_A / Q_B = A / B$.

B. Parametrization

So far two parameters were introduced in the model, x and y, the former to partition the excitation energy and the latter to partition longitudinal momentum among the three sources A, B, and C. A bounce off in the transverse direction

at the collision is described by the parameter z. This represents the transverse momentum ($A\,\text{MeV}/c$) of the abraded prefragment [30]. This complies with the observed increase of trajectory deflection [31]. There are several mechanisms that combine to contribute to the repulsion, i.e., the Pauli blocking and the Coulomb barrier.

Because the momenta transfer is a statistical process, all the values in the parametrization are taken as mean values. All three parameters x, y, and z are considered as impact parameter b and energy dependent, so we get

$$x(b) = x_o\left[1 - \left(\frac{b}{b_{\max}}\right)^2\right],$$

$$y(b) = y_o\left[1 - \left(\frac{b}{b_{\max}}\right)^2\right],$$

$$z(b) = z_o \sin^{2/3}\left(\pi\frac{b}{b_{\max}}\right), \tag{9}$$

where $b_{\max}$ is the sum of the radii of the colliding nuclei.

At lower energies the spectator parts remain relatively cold. Hence the magnitude of heat leakage x_o is set to be small [24]. The longitudinal momentum loss magnitude y_o is taken as a fit to the experimental data [23]. $\mathcal{E}_{\text{lab}}$ is the projectile kinetic energy (in units MeV/nucleon) in the laboratory system. The transverse momentum transfer magnitude is usually taken as energy independent. This approximation is valid only at higher energies where the magnitude is usually fixed at 300 MeV/c [24]. In our model, an energy-dependent parameter was used [30], while the magnitude was set to a lower value (200 MeV/c), which is more appropriate for reproducing data at lower projectile energies:

$$x_o = 0.05\Lambda,$$

$$y_o = e^{-\sqrt{\mathcal{E}_{\text{lab}}/125}}\Lambda,$$

$$z_o = 200\mu\Lambda Y, \tag{10}$$

where μ is related to the masses of the target and the projectile nucleus and is given as

$$\mu = \frac{2}{1 + \dfrac{m_P}{m_T}} \tag{11}$$

and Y is the center-of-mass rapidity of the beam

$$Y = \frac{1}{2}\log\left(\frac{1+\beta}{1-\beta}\right), \tag{12}$$

where β represents the laboratory frame velocity of projectiles in units of speed of light. Coefficient Λ needs to be introduced to make the parameter values x_o, y_o, and z_o Lorentz invariant

$$\Lambda = \frac{\beta_{\text{c.m.}}}{\beta_{\text{lab}}}\gamma_o^{-2}, \tag{13}$$

where γ_o is the Lorentz relativistic factor

$$\gamma_o = (1 - \beta_{\text{lab}})^{-1/2}. \tag{14}$$

C. Fragment ablation

After initial abrasion of the projectile the final fragment is formed from an excited cluster of projectile spectators A in one of the two scenarios. The excited prefragment can be thermalized before ablation. Hence, the prefragment becomes the final state fragment. If thermalization does not occur, the final fragment A_F is created by evaporation of mass in the form of a light fragment $\Delta A = A - A_F$. It is reported in Refs. [33,34] that the first scenario is more likely to happen.

Now let us consider the second case. We describe the excited nucleus as a Fermi gas. The average kinetic energy loss per nucleon in the center-of-mass frame is calculated by

$$\langle d\mathcal{E}_k\rangle = \mathcal{E}_{kPF} - \mathcal{E}_{kF} = \mathcal{E}_A - \mathcal{E}_{\Delta A} - \mathcal{M}_f c_o^2, \tag{15}$$

where $\mathcal{E}_{kP}$ is the projectile kinetic energy per nucleon, $\mathcal{M}_f$ is the rest mass per nucleon of fragment with kinetic energy $\mathcal{E}_{kF}$. In the Fermi gas the kinetic energy of remnant fragment with mass ΔA can be estimated with

$$\mathcal{E}_{k\Delta A}(A_F \leqslant A) = \mathcal{E}_{kA} + \frac{3}{5}\varepsilon_{\text{Fermi}} + \frac{\varepsilon_{\text{Coul}}(\Delta A, A)}{A_A}, \tag{16}$$

where $\varepsilon_{\text{Coul}}$ is Coulomb barrier in the touching sphere approximation

$$\varepsilon_{\text{Coul}} = \frac{Z_{\Delta A}Z_F e^2}{4\pi\varepsilon_o(R_{\Delta A} + R_F)}, \tag{17}$$

where R_F and $R_{\Delta A}$ are nuclear radii of final fragment and the remnant part of the prefragment, respectively. In the description of the nucleus as a Fermi gas the Fermi energy $\varepsilon_{\text{Fermi}}$ is an estimation of kinetic energy of emitted nucleon or charged particle. We calculate the energy from Fermi momenta measured by Moniz *et al.* [32]. The values for different nuclei are obtained by the following best-fit approximations to the measured values:

$$P_{\text{Fermi}} = 281\ \text{MeV}/c(1 - A^{-0.568}),$$

$$\varepsilon_{\text{Fermi}} = 100\ \text{MeV}(1 - A^{-0.1083}), \tag{18}$$

for Fermi momentum and Fermi energy, respectively. Results are given in Fig. 4. The ablation step of the reaction additionally (to the abrasion) widens the distribution of final fragment momenta (see Sec. II F for details).

D. Emission angles

The final fragment has a lower energy than the abraded prefragment. However, we assume that the distribution of the fragment emission direction is isotropic in the center-of-mass system of the prefragment. In the laboratory system the di-
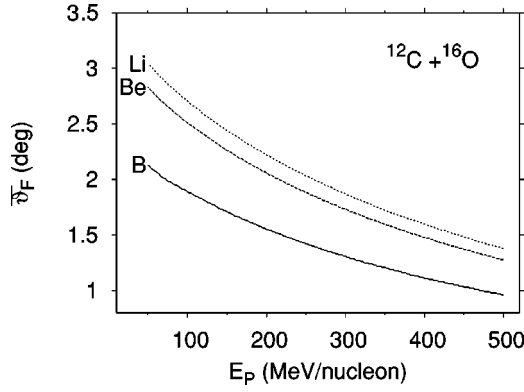
FIG. 5. Calculated average emission angles for different fragments. The example presented here is a ^{12}C projectile on an ^{16}O target atom.

rection of the final fragments would be on average the same as those of the prefragments. Thus the emission angles of the fragments are directly calculated from the longitudinal and the transverse momenta of the prefragments. Using Eqs. (3) and (9) it is possible to calculate both components of the prefragments momenta after abrasion $P_\parallel$ and $P_\perp$. The bounce-off angle of the prefragment and correspondingly the mean emission angle of the final fragment is at a specific impact parameter b calculated as

$$\vartheta_F(b) = \arctan\left(\frac{P_\perp(b)}{P_\parallel(b)}\right). \qquad (19)$$

As an example the average fragment emission angles are calculated for a ^{12}C projectile on an ^{16}O target atom and shown in Fig. 5.

E. Impact parameters and abrasion channels

Some models [24] take into account the general impact parameter averaged values of momentum transfer for all fragments. Consequently this results in same values of emission angles for fragments of different mass.

Hüfner *et al.* [33] performed a calculation of various abrasion cross sections in an abrasion-ablation reaction model. The cross sections were calculated as a function of the impact parameter. The cross sections peaked at large impact parameter when only a few nucleons were removed, while the removal of more particles occurs largely at smaller impact parameters. Hence, a similar prescription for calculating mean momenta transfer was introduced in our model.

Since at various impact parameters fragment's direct progenitor differs, in our model the abrasion step of the reaction of production of a specific fragment A_F is divided into several channels for given prefragments $A_P \rightarrow A_{PF} \rightarrow A_F$. For example, for a ^{12}C projectile the ^{8}B fragment can be produced from prefragments with a mass range from 9 to 12. To determine different abrasion channels, a geometrical calculation of the overlap volume of the colliding particles is made. Thus the dependence of the number of projectile spectators on the impact parameter is obtained

$$A_{PF} = A_P \mathcal{P}\left(\frac{R_P}{R_T}, b, E\right). \qquad (20)$$

Then, the range of values of the impact parameter $[b_{PF1}, b_{PF2}]$ is determined for which the condition in Eq. (20) is satisfied for all abrasion channels PF. Additionally, the mean impact parameter b_{PF} is calculated. The corresponding momentum transfers are calculated in the longitudinal and transverse direction, respectively,

$$P_{PF\parallel,\perp} = P_{\parallel,\perp}(b_{PF}). \qquad (21)$$

The probability Γ_{PF} for the abrasion channel A_{PF} is obtained in the following manner. First, we estimate the geometrical area (cross section) S_{PF} of the abrasion channel

$$S_{PF} = \pi(b_{PF2}^2 - b_{PF1}^2). \qquad (22)$$

Secondly, a simple statistical weighting factor e^{Q/E_{PF}^*} is used, which approximates the fragment probability from the A_{PF} channel excitation energy and separation energy for $PF \rightarrow F$. Hence,

$$\Gamma_{PF} = F_1 S_{PF} e^{Q/E_{PF}^*}, \qquad (23)$$

where F_1 is a normalization factor obtained from condition $\Sigma_{PF}\Gamma_{PF}=1$, where E_{PF}^* is the mean excitation energy of the prefragment after abrasion and is calculated according to the NUCFRG2 model by Wilson *et al.* [28]. Q is the separation energy of ablation where we assume all possible combinations of evaporated protons, neutrons, and α particle clusters. The separation energy is calculated in the following way:

$$Q = [m_{PF} - (m_F + Pm_p + Nm_n + \alpha m_\alpha)]c_o^2 - E_{\text{Coul}}, \qquad (24)$$

where m_{PF}, m_F, m_p, m_n, and m_α are standard masses for prefragment, fragment, proton, neutron, and α particle, respectively. P, N, and α are the numbers of emitted protons, neutrons, and α particles. E_{Coul} is the height of the Coulomb barrier calculated with the approximation in Eq. (17). It should also be noted that the channel A_{PF} can have several subchannels, i.e., abraded prefragments with different charges. Since we use a geometrical model all possible subchannels within one abrasion channel are considered equally probable. As the α particle is tightly bound in comparison to other nucleon arrangements, the helium production in the ablation process is maximized. All the abovementioned considerations indirectly include even-even nuclei and isospin effects. Consequently, some reaction channels Γ_{PF} are thus enhanced and others suppressed. The cross section for specific break-up reactions of light even-even projectiles is higher. Nuclei such as ^{12}C, ^{16}O, ^{20}Ne, ^{24}Mg, ^{28}Si, and ^{32}S have very low Q values for emission of α particle clusters. In the case of heavier projectiles, larger clusters can also be emitted.

F. Momentum distributions

As collisions occur at a wide range of impact parameters which lead to different deflection and momentum loss, the momentum distributions also have to be derived. The momentum distributions of the nuclides produced by fragmen-

tation of various projectiles and targets were found to be Gaussian-like [15].

Since the reaction is described in a two step abrasion and ablation model, we also divide the total spread of momentum $_{tot}\sigma$ into two parts $_{abr}\sigma$ and $_{abl}\sigma$, respectively. The momentum dispersion in the abrasion step can be derived with the following assumptions. It originates from two sources. The first stems from the various impact parameters that lead to the same final product. The variance is estimated from the geometrical prescription to determine the most probable impact parameter

$$_{abr,1}\sigma_{\parallel,\perp} = \left(\frac{dP_{\parallel,\perp}}{db}\right)_{b_{mp}} \sigma_b, \tag{25}$$

where the width of the impact parameter distribution is estimated as $\sigma_b = (b_{PF2} - b_{PF1})/2$ from Eq. (20). The second source is associated with intranuclear interaction during the abrasion overlapping. For the given impact parameter the target chord $l_{\parallel,\perp}$ through the participant region is calculated as used in Ref. [28]. The spread is estimated by taking into account the mean-free path of the nucleons λ as

$$_{abr,2}\sigma_{\parallel,\perp} = \Delta P_{\parallel,\perp} \sqrt{\frac{\lambda}{l_{\parallel,\perp}}}, \tag{26}$$

where $\Delta P_{\parallel,\perp}$ is the prefragment's momentum change in the longitudinal and transverse direction. $_{abr,2}\sigma_{\parallel,\perp}$ implies that more central collisions have a larger momentum spread.

In the abrasion-ablation picture the final fragment is produced by the ablation of the excited prefragment. The evaporation of the final fragment A_F is isotropic in the prefragment's moving frame. The calculation of the ablation momentum spread is performed in a statistical manner according to Goldhaber [37]. The fragment's r.m.s. momentum $(\langle P_{A_F}^2\rangle)^{1/2}$ in the prefragment's moving frame is equal to the ablation spread of the fragment's momentum in the projectile-target c.m.s. With the assumption of a post-collision equilibrated system, the predicted width of the momentum distribution is

$$\langle P_{A_F}^2\rangle = P_F^2 \frac{A_F(A_{PF} - A_F)}{A_{PF} - 1}, \tag{27}$$

where A_{PF} and A_F are the mass numbers of the prefragment and final fragment, respectively. P_F is the relative momentum of the fragment calculated according to the approximation in Eq. (15). Variance $\langle P_{A_F}^2\rangle$ has a parabolic dependence on the fragment mass. Additionally, the ablation component of the momentum spread can be written as a sum of projections (parallel and perpendicular) to the impinging projectile axis. Due to isotropic emission in the prefragment's moving frame, the spread in the longitudinal and transverse direction are on average the same, $_{abl}\sigma_{\parallel} \approx {}_{abl}\sigma_{\perp}$

$$\langle P_{A_F}^2\rangle = {}_{abl}\sigma_{\parallel}^2 + {}_{abl}\sigma_{\perp}^2 \Rightarrow {}_{abl}\sigma_{\parallel,\perp} = \frac{P_F}{\sqrt{3}}\sqrt{\frac{A_F(A_{PF} - A_F)}{A_{PF} - 1}}. \tag{28}$$
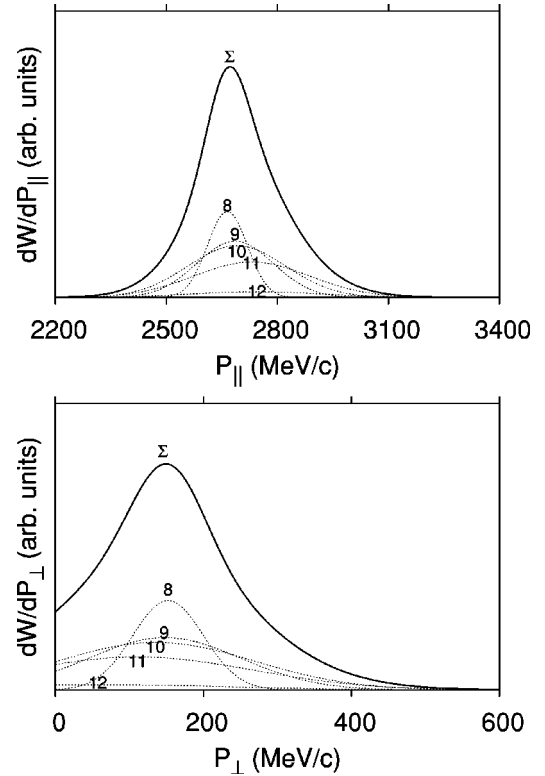

FIG. 6. Model calculated momentum transfer distributions for different abrasion channels. Dotted lines depict weighted distributions for production of the ^{8}B isotope through all possible abrasion channels. Each channel is labeled with the mass number of the corresponding prefragment. The sum of all channels is depicted by a full line. The example presented is the collision of a 70 MeV/nucleon ^{12}C projectile on an ^{16}O target atom.

Hence the total spreads of the longitudinal and the transverse momenta are obtained as the sums of the abrasion and ablation parts

$$_{tot}\sigma_{\parallel}^2 = \frac{m_F}{m_{PF}}{}_{abr}\sigma_{\parallel}^2 + {}_{abl}\sigma_{\parallel}^2,$$

$$_{tot}\sigma_{\perp}^2 = \frac{m_F}{m_{PF}}{}_{abr}\sigma_{\perp}^2 + {}_{abl}\sigma_{\perp}^2. \tag{29}$$

As fragments from different prefragments A_i have different momentum widths $_{tot}\sigma(A_i)$, an appropriate weighted averaging has to be performed. The total distribution of momenta is hence the sum of Gaussians with an appropriate statistical weighting factor for each channel

$$\frac{dW}{dP} = \sum_{PF=A_F}^{A_P} \Gamma_{PF} \frac{1}{\sigma_{PF}\sqrt{2\pi}} e^{-(P - P_{PF})^2/2\sigma_{PF}^2}. \tag{30}$$

Figure 6 shows a detailed plot of the final fragment momentum distribution for each specific abrasion channel. The sum distribution for a specific final fragment isotope is also obtained according to Eq. (30). As an example the reaction ^{12}C + ^{16}O $\rightarrow$ ^{8}B + X is presented.
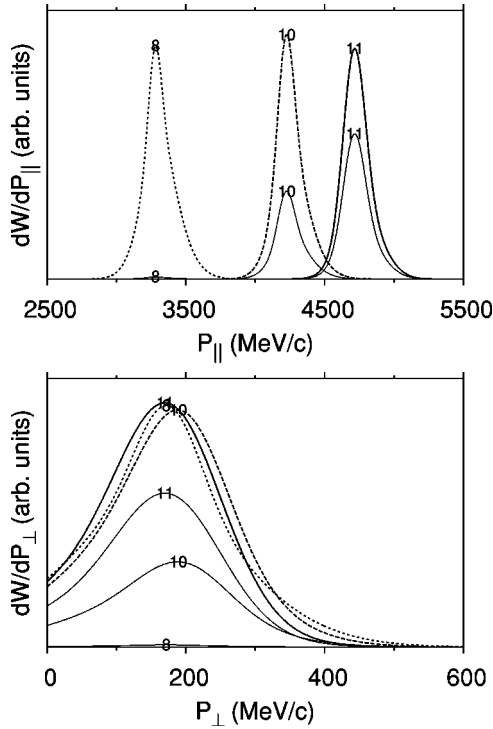
FIG. 7. Model calculated momentum transfer distributions and corresponding distribution of fragment emission angles. The example presented is a collision of a 100 MeV/nucleon ^{12}C projectile on an ^{16}O target atom. Momentum distributions are calculated for production of different nitrogen fragments isotopes and plotted with dotted lines. Full lines represents the momentum distribution for each isotope but weighted by an appropriate production factor. The factors are calculated with a partial reaction cross section model [35], which is an improved version of the model described in Ref. [36].

Figure 7 shows as an example the calculated momentum distribution of boron fragments produced in the collision of a ^{12}C projectile and an ^{16}O target atom. From the distributions in the longitudinal and transverse directions the distribution of fragment emission angles can be obtained.

III. PERIPHERAL COLLISIONS

Now let us consider peripheral collisions for larger impact parameters b where no nuclear interaction occurs. Reactions are possible due to the strong long range electromagnetic fields which are produced over a very short time scale in relativistic heavy ion collisions. These electromagnetic pulses increase in strength with energy because of the Lorentz contraction.

A typical time sequence of a Coulomb interaction leading to fragmentation of a projectile is shown schematically in Fig. 8. When approaching the target nucleus the projectile is first deflected in the target's electric field. Electromagnetic dissociation occurs when a virtual photon is exchanged between the target nucleus and the projectile. The usual result of this process is energy transfer to the harmonically bound charge in the projectile nucleus. For high-Z nuclei the mode of deexcitation is primarily by neutron emission. Charged-
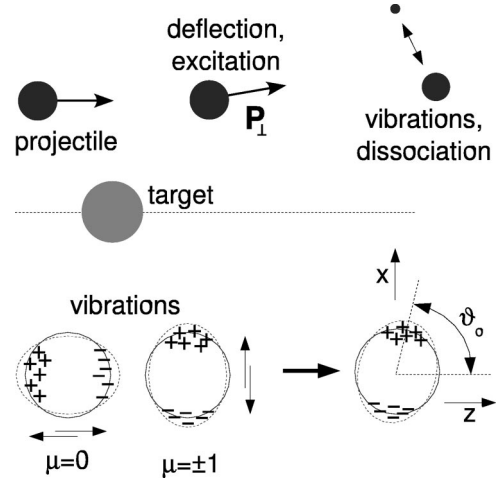

FIG. 8. Peripheral collision of projectile and target in the laboratory frame. Impact parameter b is larger than the sum of the radii of the two nuclei. When passing by, the projectile is slightly deflected in the electric field of the target ion. Additionally, the projectile is excited (induced proton and neutron vibrations), which can result in subsequent dissociation of the nucleus.

particle emission is hindered as a result of the Coulomb barrier, but can become more probable for low-Z nuclei.

In analogy to nuclear collisions we can describe Coulomb collisions by a two-step reaction model; deflection-excitation and vibration-dissociation of the projectile.

A. Deflection and excitation

A fast charged particle incident on matter makes collisions with the atomic electrons and nuclei. If the particle is heavier (proton, etc.), the collisions with electrons and with nuclei have different consequences. The light ions can take up appreciable amounts of energy from the incident particle without causing significant deflections, whereas the massive nuclei absorb very little energy but because of their greater charge cause scattering of the incident particle. Thus energy loss by the incident particle occurs almost entirely from its incident collisions with electrons. The deflection of the particle from its incident direction, on the other hand, results from essentially elastic collisions with atomic nuclei.

When describing fragmentation events the collision time of the projectile with the target nucleus is very short (in the order of 10^{-23} s). Thus energy loss effects due to electron interaction can be neglected. The passage of a particle with charge Z_P, velocity v, and impact parameter b (larger than the nuclear interaction radius) by a target nucleus at rest will predominantly cause a momentum change of the charged constituents of the nucleus, i.e., the protons. For not overly close collisions the momentum in the transverse direction (see Fig. 8) is given in the classical approximation at relativistic energies [38] by

$$P_{\mathrm{def}} = 2\frac{Z_P Z_T e^2}{4\pi\epsilon_0 b v}. \tag{31}$$

At the same time some of the energy is transferred into internal excitation of the projectile. The probability for the

Coulomb excitation of a nuclear state becomes larger the longer is the transition time τ compared with the interaction time t_{coll}. The transition time is given as

$$\tau = \hbar/E_S = 1/\omega, \tag{32}$$

where E_S is the energy level of the excited state The interaction time t_{coll} in the collision is estimated by the half-distance of closest approach a and projectile velocity v_P as

$$t_{\text{coll}} = \frac{R}{\gamma v_P} \tag{33}$$

taking into account the relativistic contractions by means of the Lorentz factor. R is the sum of the radii of the colliding nuclei, the shortest distance at which the nuclei interact only electromagnetically.

To calculate the excitation energy of the passing projectile we can use the vibrator model for the nucleus [38], where the energy transferred to a harmonically bound nucleon is calculated. Furthermore the nucleus is described as a sum of harmonic oscillators which gives the projectile excitation energy as [39]

$$E*(b) = \frac{2E_S^2}{u}\alpha^2 \frac{Z_T^2 Z_P(A_P - Z_P)}{A_P}\left(\frac{c}{v}\right)^4$$

$$\times \frac{1}{\gamma^2}\left(K_1^2(x) + \frac{1}{\gamma^2}K_0^2(x)\right), \tag{34}$$

where u is the atomic mass unit, v is the speed of the target (measured from the projectile rest frame), $\gamma = [1 - (v/c)^2]^{-1/2}$ is the Lorentz factor, and α is the fine structure constant

$$\alpha = e^2/4\pi\epsilon_0\hbar c = 7.297 \times 10^{-3}, \tag{35}$$

$\hbar$ is the Planck constant, K_n are modified Bessel functions, and x is defined as

$$x = \omega b/\gamma v. \tag{36}$$

From the calculation of excitation energy [Eq. (34)], one can also interpret the probability $W_{\text{exc}}(b)$ of exciting the vibrational state in a collision with impact parameter b as

$$W_{\text{exc}}(b) = \frac{E*(b)}{E_S}. \tag{37}$$

In Ref. [39] it was noted that the excitation probabilities in peripheral heavy ion collisions approach unity at grazing impact parameters (very close to the nuclear interaction radius). But calculations performed for light systems in the energy region <1 GeV/nucleon (of importance for radiotherapy and space dosimetry research) revealed that excitation is a highly improbable event (compared to nuclear fragmentation by several orders of magnitude). Due to their quadratic dependence on target charge, these events play a notable role only for very heavy targets (e.g., Pb).

B. Vibration and dissociation

In the excited state large proton and neutron excesses are developed at the surface. Figure 8 shows that vibrations can
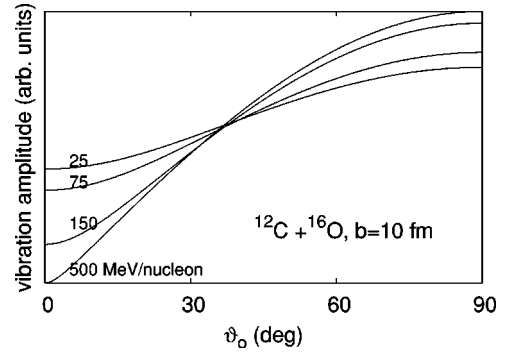

FIG. 9. Angular distribution of vibration direction at different energies. The distribution functions at each energy are normalized so that the function integral equals 1.

be generated in different modes. $\mu = 0$ corresponds to the action of the electric field component parallel to the impinging direction of the projectile. The perpendicular component of the electric field generates $\mu = \pm 1$ vibrations and because of symmetry the excitation probability must be equally distributed between the states ± 1.

From the dynamics of the electromagnetic excitation process, the angular distribution of fragments can be calculated [39]. The fragment emission direction corresponds to direction of the vibration amplitude A

$$A(\vartheta_o) \sim \sqrt{K_1^2(x)\sin^2\vartheta_o + \frac{1}{\gamma^2}K_0^2(x)\cos^2\vartheta_o}, \tag{38}$$

where ϑ_o is the polar angle in the projectile's moving frame, where the z axis coincides with the impinging direction in the laboratory system (see Fig. 8). Angular distributions for a $^{12}\text{C} + ^{16}\text{O}$ colliding system at an impact parameter of 10 fm are plotted for different projectile energies in Fig. 9. At higher energies there is a strong tendency for emission perpendicular to the beam axis, while at lower energies the emission is almost isotropic in the projectile moving frame.

C. Fragment momentum distributions and emission angles

We assume that in the deflection step the incident momentum of the projectile P_o does not change,

$$\Delta P_{\parallel} \approx 0. \tag{39}$$

The momentum due to Coulomb repulsion is perpendicular to the beam and is given in Eq. (31). Now let us consider a projectile fragmentation process $P \rightarrow F + \tilde{F}$, a decay into the final fragment F and the remnant part. Typically in Coulomb excitation the projectile emits one or several nucleons (either as a cluster or small light nuclei), therefore $F \sim P$ and $\tilde{F} \ll F$. The mass spectrum of fragments is much narrower than the fragments produced in direct collisions. The momentum of the fragment ($P_{F1} = P_{F2}$) obtained from the decay of the excited vibration state is given by

$$P_{\text{diss}} = \sqrt{2m_o\Delta E}, \tag{40}$$

where m_o is the reduced mass of $F + \tilde{F}$

$$m_o = \frac{m_1 m_2}{m_1 + m_2}, \tag{41}$$

where m_1 and m_2 are the masses of fragments F and $\tilde{F}$, respectively. ΔE is the decay energy, i.e., the excitation energy above the threshold for the reaction

$$\Delta E = E_S - Q. \tag{42}$$

Q is the separation energy calculated as in Eq. (24).

The final momentum of the fragment (longitudinal and transverse component, respectively) is thus

$$P_{F\parallel} = \left\{ \begin{array}{c} \dfrac{m_F}{m_P} P_o + P_{\text{diss}} \cos \vartheta_o \\[2mm] \dfrac{m_F}{m_P} P_o - P_{\text{diss}} \cos \vartheta_o \end{array} \right\}, \tag{43}$$

$$P_{F\perp} = \left\{ \begin{array}{c} \dfrac{m_F}{m_P} P_{\text{dif}} + P_{\text{diss}} \sin \vartheta_o \\[2mm] \dfrac{m_F}{m_P} P_{\text{def}} - P_{\text{diss}} \sin \vartheta_o \end{array} \right\}. \tag{44}$$

Momenta are double valued, where each value is equally probable due to the symmetry of decay of the vibrating projectile. The fragment is emitted either in the ϑ_o or in $\pi - \vartheta_o$ direction.

To obtain the widths of the momenta distribution we will use a two step reaction methodology in analogy to direct collisions (see Sec. II F). For the deflection-excitation step the assumption for longitudinal momentum spread $\sigma_{P_o} \approx 0$ can be made from Eq. (39). Calculations from Eq. (34) show that excitation and potential disintegration occurs at the grazing impact parameter and the probability drops sharply for increasing impact parameters ($\sim b^{-2}$). A very narrow interval of b has to be taken into account. Hence, the transverse momentum spread on deflection can also be estimated as $\sigma_{P_{\text{def}}} \approx 0$.

The main contribution to momentum spread originates in the different emission directions of fragments in their moving frame. $\sigma_{\text{diss}\perp}$ and $\sigma_{\text{diss}\parallel}$ are obtained from the vibration amplitude angular distribution in Eq. (38).

IV. CONCLUSION

A new semiempirical model for fragment emission angles in light and heavy ion fragmentation reactions was developed. The aim of the model is to describe reactions for systems in the energy region relevant for radiotherapy and space-flight dosimetry research (from a few 10 MeV/nucleon to a few GeV/nucleon). Recent measurements [8] have shown the the straight-ahead approximation (fragments travelling in the same direction with the same velocity) is oversimplified and does not conform with observations at lower energies, where the fragment emission angles are larger. The model is applicable to description of fragmentation events of ions from carbon to iron on different target materials (water, plexiglas, polyethylene, aluminium, etc.). Emission angles are calculated for heavier and lighter fragments, but the model cannot be used for protons and neutrons. Contributions from both central and peripheral collisions were investigated, where fragmentation due to nuclear and Coulomb interaction occurs, respectively.

For central collisions the reaction is described by a two step abrasion-ablation model, where the collision parameters are determined from a simple geometrical model with appropriate corrections. For the first time, the consequences for emission angles from both steps, abrasion and ablation, were strictly analyzed. During the abrasion part of the reaction a prefragment is formed, where at collision a loss of longitudinal momentum and an uptake of transverse momentum occurs. In the ablation stage the final fragment is formed. We assume that the same fragment can be formed through different abrasion channels, which results in different momenta transfers and momentum distribution widths.

For peripheral collisions the Coulomb excitation of nucleon vibration resonances and subsequent decay into fragments is taken into account. Fragment emission angles were calculated from deflection in the electric field and from the direction of vibrations in excited nuclear states. However, calculation of the probability of such events in the systems included in our study showed that Coulomb fragmentation can be neglected (nuclear fragmentation is several orders of magnitude higher). It only plays an important role at higher energies ($E >$ a few 10 GeV/nucleon) and/or for heavier targets ($\gg$Fe).

With the recent developement of experimental methods using etched track detectors and trajectory-tracing techniques, measurement of relative emission angles have become available. Details will be published in a subsequent paper.

[1] A. Chatterjee and T. H. Borak, Phys. Medica **17**, 49 (2001).

[2] G. Kraft, *The Physics of Multiply and Highly Charged Ions, Radiobiological Effects of Highly Charged Ions* (Kluwer Academic, Dordrecht, 2003).

[3] K. Kawachi, T. Kanai, M. Endo, Y. Hirao, and H. Tsunemoto, J. JASTRO **1**, 19 (1989).

[4] Y. Hirao and H. Ogawa, Nucl. Phys. **A538**, 541c (1992).

[5] G. Kraft *et al.*, Nucl. Tracks Radiat. Meas. **19**, 911 (1991).

[6] J. W. Wilson, S. Y. Chun, F. Badavi, L. Townsend, and S. L. Lamkin, NASA Technical Paper 3146, NASA, Langley Research Center, Hampton, Virginia, 1991.

[7] L. Sihver, D. Schardt, and T. Kanai, Jpn. J. Med. Phys. 18, 1 (1998).

[8] M. Giacomelli, J. Skvarč, R. Ilić, L. Sihver, and N. Yasuda, Radiat. Meas. **36**, 329 (2003).

[9] M. Scholz, Nucl. Instrum. Methods Phys. Res. B **161–163**, 76 (2000).

[10] D. Schulz-Ertner, T. Haberer, M. Scholz, C. T. F. Wenz, O.

Jäkel, G. Kraft, M. Wannenmacher, and J. Debus, Radiother. Oncol. **64**, 189 (2000).

[11] B. Golovkov, D. Aleksandrov, L. Chulkov, G. Kraus, and D. Schardt, Adv. Hadron Therapy, Int. Congr. Series **1144**, 316 (1997).

[12] K. Gunzert, Diplomarbeit, Technische Universität Darmstadt, 2000.

[13] S. Momota *et al.*, Nucl. Phys. **A701**, 150c (2002).

[14] R. G. Stokstad, Comments Nucl. Part. Phys. **13**, 231 (1984).

[15] D. J. Morrisey, Phys. Rev. C **39**, 460 (1989).

[16] P. B. Price and Y. D. He, Phys. Rev. C **43**, 835 (1991).

[17] W. Heinrich *et al.*, Radiat. Meas. **25**, 203 (1995).

[18] J. D. Bowman, W. Swiatecki, and C. Tsang, LBL 2908, Lawrence Berkley Laboratory, University of California, 1973.

[19] J. Vervier, J. Äystö, H. Doubre, S. Gales, G. Morrison, G. Ricco, D. Schwalm, and G. E. Körner, NuPECC Report, NuPECC, 1997.

[20] G. D. Westfall, J. Gosset, P. J. Johansen, A. M. Poskanzer, W. G. Meyer, H. H. Gutbrod, A. Sandoval, and R. Stock, Phys. Rev. Lett. **37**, 1202 (1976).

[21] G. R. Choppin, J. Liljenzin, and J. Rydberg, *Radiochemistry and Nuclear Chemistry* (Butterworth-Heinemann, Boston, 2001).

[22] G. Fai and J. Randrup, Nucl. Phys. **A404**, 551 (1983).

[23] G. Fai and J. Randrup, Comput. Phys. Commun. **42**, 385 (1986).

[24] C. H. Tsao, R. Silberberg, A. F. Barghouty, and L. Sihver, Astrophys. J. **451**, 275 (1995).

[25] J. Gosset, H. H. Gutbrod, W. G. Meyer, A. M. Poskanzer, A. Sandoval, R. Stock, and G. D. Westfall, Phys. Rev. C **16**, 629 (1977).

[26] H. de Vries, C. de Jager, and C. de Vries, At. Data Nucl. Data Tables **36**, 495 (1987).

[27] E. Wesołowski, J. Phys. G **10**, 321 (1984).

[28] J. W. Wilson, R. Tripathy, F. Cucinotta, J. Shinn, F. Badavi, S. Y. Chun, J. Norbury, C. Zeitlin, L. Heilbronn, and J. Miller, NASA Technical Paper 3533, NASA, Langley Research Center, Hampton, Virginia, 1995.

[29] G. Audi and A. H. Wapstra, Nucl. Phys. **A595**, 409 (1995).

[30] A. F. Barghouty, G. Fai, and D. Keane, Nucl. Phys. **A535**, 715 (1991).

[31] K. van Bibber *et al.*, Phys. Rev. Lett. **43**, 840 (1979).

[32] E. J. Moniz, I. Sick, R. R. Whitney, J. R. Ficenec, R. D. Kephart, and W. P. Trower, Phys. Rev. Lett. **26**, 445 (1971).

[33] J. Hüfner, K. Schäfer, and B. Schürmann, Phys. Rev. C **12**, 1888 (1975).

[34] G. Peilert, H. Stöcker, and W. Greiner, Rep. Prog. Phys. **57**, 533 (1994).

[35] L. Sihver (unpublished).

[36] L. Sihver, C. H. Tsao, R. Silberberg, T. Kanai, and A. F. Barghouty, Phys. Rev. C **47**, 1225 (1993).

[37] A. S. Goldhaber, Phys. Lett. **53B**, 306 (1974).

[38] J. D. Jackson, *Classical Electrodynamics* (Wiley, New York, 1975).

[39] G. Baur and C. Bertulani, Phys. Rev. C **34**, 1654 (1986).